Discussion

Temporal and spectral hybrid interference from phase transition of Eu^{3+}/Pr^{3+}: YPO_4 and evolution of amplifier and multiplexer

Sifan Li [a], Habib Ullah [a,b], Yisha Qin [a], Zhili Chen [a], Jinyang Li [c], Yuan Zhao [a,*], Yanpeng Zhang [a,*]

[a] Key Laboratory for Physical Electronics and Devices of the Ministry of Education, Shaanxi Key Lab of Information Photonic Technique, Xi'an Jiaotong University, Xi'an 710049, China
[b] Smart Computational Imaging (SCI) Laboratory, Nanjing University of Science and Technology, Nanjing, Jiangsu Province 210094, China
[c] School of Material Science and Engineering, Shaanxi Key Laboratory of Green Preparation and Functionalization for Inorganic Materials, Shaanxi University of Science and Technology, Xi'an, 710021, China

ARTICLE INFO

ABSTRACT

We study the temporal and spectral oscillation originated from the interference between the fluorescence (FL) and spontaneous parametric four-wave mixing (SP-FWM) signals. The FL and SP-FWM are generated from different phases of Eu^{3+} or Pr^{3+} doped YPO_4 under the nonlinear SP-FWM process. We discuss and compare the spectral interfering oscillations and self-Rabi oscillations controlled via multiple phase transitions (hexagonal-phase and mixed-phase) of Eu^{3+}: YPO_4 and Pr^{3+}: YPO_4. The coexistence mechanism of interference and self-oscillations in time domain is also investigated. Further, we discuss the cross-Rabi oscillation in correlated light beams, which evolves from FL signal (having Sinc profile) to SP-FWM (having Cosine profile) in the hybrid signal regime. Based on these results, we have realized wavelength division multiplexing, and temporal amplifier with the temporal interference being controlled by the gate position, and frequency detuning. Our experimental results provide a technique to achieve higher channel equalization ratio about 85%.

© 2021 Elsevier B.V. All rights reserved.

1. Introduction

In recent decades, quantum coherence excitation and coherence transfer have been thoroughly studied in atomic gases. These processes lead to many important physical phenomena. Compared with atomic gases, atomic coherence-induced effects in solid materials are very attractive for practical applications. Rare-earth orthophosphates matrix doped with trivalent ions (like Pr^{3+}: YPO_4, Eu^{3+}: YPO_4) are more suitable for practical applications due to their unique physical, chemical, and structural properties. These properties make them suitable candidates for luminescent materials [1][2], which play a significant role in optical communication, optical microscopy, displaying information [3][4], and quantum optics. In Yttrium phosphate crystal YPO_4 crystal, the "atom-like" properties of the dopant can be kept, due to which the atomic coherence can be induced easily when interacting with multiple laser beams. Research on light coherent storage, all-optical routing [5], optical velocity reduction and reversible storage of double light pulses [6], enhanced four-wave mixing, all-optically controlled higher-order fluorescence (FL), has been reported in YPO_4. Such crystals have potential applications in optical devices such as transistors, routers, filters, etc. The YPO_4 crystal exists in two polymorphic forms, i.e., hexagonal (H) and tetragonal (T) [7][8]. Specifically, the hexagonal phase has a P6222 space group with a rhabdophane-type structure where Y^{3+} ions occupy a D2 point-group symmetry site [9], while the tetragonal phase has an I41/amd space group, where Y^{3+} ions occupy a D2d point-group, and two kinds of coordination bonds [10].

Interference is a well-known effect to understand the coherence and superposition in quantum physics [11][12] and it provides a solid foundation for the development of the coherence and the quantum theory of light [13]. First and second-order interference is defined [14] between two different independent sources, i.e., thermal and laser light. It was found that ghost imaging can be realized experimentally with chaotic thermal light [15][16]. Bennink *et al.* showed that ghost imaging technique does not require entanglement and provided an experimental demonstration with a classical source [17]. Compared to two-photon entangled sources, the disadvantage of classical light in ghost imaging is the limited visibility [18]. Dirac considered superposition comes only from the single

* Corresponding authors.
  E-mail addresses: zhaoyuanlg@mail.xjtu.edu.cn (Y. Zhao),
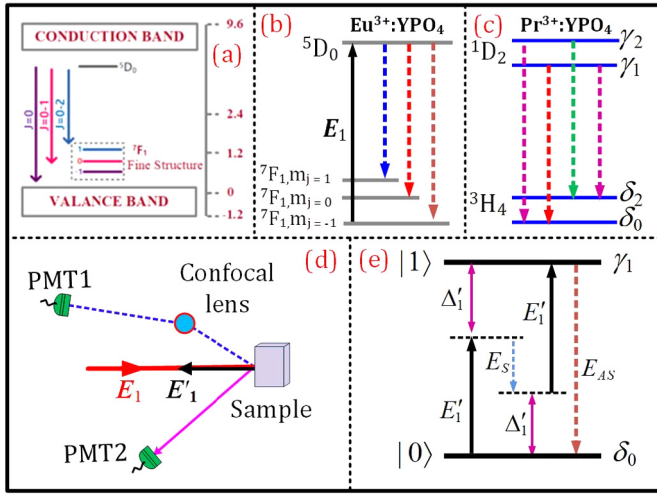 ypzhang@mail.xjtu.edu.cn (Y. Zhang).

Fig. 1. (a) shows the fine structure of energy levels of Eu^{3+}: YPO_4. (b) shows two-level systems in Eu^{3+}: YPO_4 excited by two laser beams. (c) shows a two-level system in Pr^{3+}: YPO_4. (d) shows the experimental setup and (e) shows the schematic diagram of FWM in a two-level system.

photon in the single photon interference [19]. According to the superposition principle in Feynman's path integral theory [20], two-photon interference is not the interference between two individual photons, but the interference resulting from different Feynman paths [21]. However, in Haijun Tang's article [22], the interference between the three multi-order fluorescence (MFL) signals at room temperature is realized by nonlinear interaction. Similarly, the hybrid interference between the fluorescence (FL) and spontaneous parametric four-wave mixing (SP-FWM) signals in this article can also be realized by nonlinear interaction.

In this paper, we discuss the oscillations originated from the interference of FL and the coherent outputs from Eu^{3+}/Pr^{3+}: YPO_4 in both time and spectral domains of the nonlinear SP-FWM process. Interference is high when the emission of FL and coherent (Stokes (E_S) and anti-Stokes (E_{AS})) have equal contributions in the hybrid signal regime. We further evaluate the interference and self Rabi-oscillations coexisting in the spectral and temporal intensity of the hybrid signal regime. Spectral oscillations from different phases of Eu^{3+}: YPO_4 and Pr^{3+}: YPO_4 are also discussed. Such results are employed to realize the wavelength division multiplexing (WDM) of classical and coherent channels, and temporal amplifier. The cross-Rabi oscillation is found in the two-mode intensity-noise correlation of E_S/E_{AS} and the hybrid FL signals. The evolution of FL profile (Sinc function) to SP-FWM profile (Cosine function) is discussed when power is changed from high to low.

2. Experimental setup and basic theory

In this experiment, the sample is held in a cryostat (CFM-102) at 77 K (due to low phonon effect, strong dressing effect) and the temperature is controlled by flowing liquid nitrogen. The sample has 5% concentration of doped Eu^{3+}/Pr^{3+} ions in a host YPO_4 crystal. To generate the pumping field E_i (ω_i, Δ_i), a tunable dye laser (narrow scan with a 0.04 cm^{-1} linewidth) is pumped by an injection-locked single-mode Nd: YAG laser (Continuum Power lite DLS 9010, 10 Hz repetition rate, 5 ns pulse width). Here $\Delta_i = \Omega_{mn} - \omega_i$ is the frequency detuning, where Ω_{mn} is the corresponding atomic transition frequency between levels and ω_i (i = 1,2) is the laser frequency. Fig. 1(a) shows the crystal field splitting of the fine structure of Eu^{3+}: YPO_4 crystal. The Eu^{3+}: YPO_4 has a ground state ($^7F_1$) and an excited state ($^5D_0$), where the ground state $^7F_1$ is split into three fine-structure sub-levels, i.e., $m_{j=0}$ and $m_{j=\pm1}$, (Fig. 1(b)) under the action of the crystal field

of YPO_4. Fig. 1(c) shows the energy level of Pr^{3+}: YPO_4 crystal. In Pr^{3+}: YPO_4, under the action of crystal field and site symmetry, the (2J + 1) degeneracy is partially lifted and $^3H_4$ (ground state) and $^1D_2$ (excited state) levels are split into seven and four Stark levels respectively. The allowed transitions for Pr^{3+} in YPO_4, energy levels of $^3H_4$, and $^1D_2$ can be reduced to 2 levels, labeled as δ_0, δ_2, γ_1 and γ_2 in Fig. 1(c). Fig. 1(d) shows the schematic diagram of our experimental setup, where the pumping field E_1 excites the sample and is reflected (E_1') back from the surface of the crystal with a small angle θ. The E_S and E_{AS} signals are generated from the reflected beam E_1' (ω_1', Δ_1') via SP-FWM process, satisfying the phase-matching conditions $k_S = k_1' + k_1' - k_{AS}$ and $k_{AS} = k_1' + k_1' - k_S$, where k_1' represents the wave vector of the reflected field E_1' and $k_{S,AS}$ is the wave vector of generated E_S and E_{AS} fields. The two photomultiplier tubes (PMT1 and PMT2) through boxcar are placed to detect the generated FL, E_S and E_{AS} signals generated by the reflected field E_1'. The boxcar gate controls the measuring range of time and determines the energy level resolution by fixing gate width (integration duration) and gate position (time delay). Change in gate position (GP) is equivalent to that in energy levels of different lifetimes. One can obtain output signals from different energy levels with different lifetimes by controlling the position of the boxcar gate. Further, gate width can be varied to control emissions from the number of energy levels. If the gate width is narrow enough, the observed signal could result from a single energy level with a single lifetime. Since the FL, E_S and E_{AS} signals have different buildup times and decay rates, they can be easily distinguished at PMT1 or PMT2 using a boxcar gate position. By fixing the gate width narrow, the observed signal comes from a single energy level having a single lifetime, which results in a strong dressing effect. Broad gate width includes the effect of many energy levels that have various lifetimes and scattering which neutralizes the dressing effect. To get a strong dressing effect, we used a narrow gate width (100 ns) in our experiment. The spectral domain signal is obtained at a computer by scanning the laser frequency, whereas the time domain intensity signal is obtained at a time-resolved oscilloscope by fixing the laser frequency at a resonant wavelength [23]. Further, in our experiment, PMT1 detects the generated hybrid signal H_1 (FL + E_S) via a confocal lens (near detector), while the detector PMT2 detects the hybrid signal H_2 (FL + E_{AS}). Due to the confocal lens, FL emission at PMT1 is more than E_S in hybrid signal H_1, whereas at PMT2, E_{AS} emission is more than FL in a hybrid signal H_2. The more emission of E_{AS} in H_2 is subjected to a far position of PMT2 without a focal setup. The schematic diagram of four-wave mixing (FWM) is illustrated in Fig. 1(e) [24].

3. Theoretical model

In a two-level system (Fig. 1(e)), by opening the laser field E_1, the E_S and E_{AS} signals are generated under the phase-matching conditions. The perturbation chains for E_S and E_{AS} signals in the two-level system are $\rho_{00}^{(0)} \xrightarrow{E_1'} \rho_{10}^{(1)} \xrightarrow{E_s} \rho_{00}^{(2)} \xrightarrow{E_1'} \rho_{10(S)}^{(3)}$ and $\rho_{00}^{(0)} \xrightarrow{E_1'} \rho_{10}^{(1)} \xrightarrow{E_{AS}} \rho_{00}^{(2)} \xrightarrow{E_1'} \rho_{10(AS)}^{(3)}$, respectively.

$$\rho_{10}^{(3)} = \frac{-iG_{AS}\left|G_1'\right|^2}{(\Gamma_{10}+i\Delta_1')(\Gamma_{00}+i\Delta_1'+\left|G_1'\right|^2/(\Gamma_{00}+i\Delta_1'))\Gamma_{11}}$$
$$= \rho_S^{(3)} = \left|\rho_{10}^{(3)}\right|\exp(i\theta_S) \qquad (1)$$

$$\rho_{10}^{(3)} = \frac{-iG_S\left|G_1'\right|^2}{(\Gamma_{10}+i\Delta_1')(\Gamma_{00}-i\Delta_1'+\left|G_1'\right|^2/(\Gamma_{00}+i\Delta_1'))\Gamma_{11}}$$
$$= \rho_{AS}^{(3)} = \left|\rho_{10}^{(3)}\right|\exp(i\theta_{AS}) \qquad (2)$$

The linewidth of the measured SP-FWM signal is $\Gamma_{S/AS} = \Gamma_{00} + \Gamma_{10} + \Gamma_{11}$. The temporal intensity of the Stokes and anti-Stokes signals are given by [25]

$$\langle I_S \rangle = 7e^{-2\Gamma_{00}t_S} + e^{-2\Gamma_{10}t_{AS}}$$
$$- 2\cos[(\Delta_2 + |G_1|^2/\Gamma_{00})t_S]e^{-(\Gamma+\Gamma_{20})t_S} \qquad (3)$$

$$\langle I_{AS} \rangle = e^{-2\Gamma_{00}t_{AS}} + e^{-2\Gamma_{20}t_S}$$
$$- 2\cos[(\Delta_1 + |G_1|^2/\Gamma_{00})t_{AS}]e^{-(\Gamma+\Gamma_{10})t_{AS}} \qquad (4)$$

The decay rate Γ for Eqs. (3) and (4) is defined as $\Gamma = (|G_1|^2 - \Delta_1\Gamma_{00} + 3\Gamma_{00}\Gamma_{10})/4\Gamma_{00}$. In a two-level system, with a strong pumping field E_1 switched on, the second-order FL signal is generated through the perturbation chain $\rho_{00}^{(0)} \xrightarrow{E_1} \rho_{10}^{(1)} \xrightarrow{-E_1} \rho_{11}^{(2)}$, the diagonal density matrix element is given by

$$\rho_{FL}^{(2)} = \frac{-|G_1|^2}{(\Gamma_{10} + i\Delta_1 + |G_1|^2/\Gamma_{00})(\Gamma_{11} + |G_1|^2/(\Gamma_{10} + i\Delta_1))}$$
$$= \rho_{FL}^{(2)} = \left|\rho_{11}^{(2)}\right| \exp(i\theta_{FL}) \qquad (5)$$

where $|G_1|^2/(\Gamma_{ij} \pm i\Delta_1)$ is the interaction between the dressing and phonon effects, $G = \mu E/\hbar$ is Rabi frequency of field E_1 with the electric dipole matrix elements μ_{ij} of levels $|i\rangle$ and $|j\rangle$, and Γ_{ij} is the transverse decay rate. The linewidth of FL is $\Gamma_{FL} = \Gamma_{10} + \Gamma_{11}$. The temporal intensity of FL is given as $I(t) = \rho_{11}^{(2)}\exp(-\Gamma_{FL}t)$.

The oscillations observed in the temporal and the spectral intensity signal results from interference between FL and E_S in the hybrid signal regime. The gate position controls the decay rates Γ_{FL} and Γ_{SPFWM}, which determine the spectral oscillations. The interference of ρ_{FL} and ρ_{SPFWM} can be calculated by Eq. (6).

$$|\rho|^2 = \left|\rho_{11}^{(2)}\right|^2 + \left|\rho_{S/AS}^{(3)}\right|^2 + 2\left|\rho_{11}^{(2)}\right|\left|\rho_{S/AS}^{(3)}\right|\cos(\theta_{FL} - \theta_{S/AS}). \quad (6)$$

Interference contrast (C) is the maximum and minimum interference between incoherent and coherent signals in a hybrid signal. As $I_{(FL)} \propto \left|\rho_{11(FL)}^{(2)}\right|^2$ and $I_{(S/AS)} \propto \left|\rho_{S/AS}^{(3)}\right|^2$, the interference contrast C can be calculated by Eq. (7).

$$C = \left|\left|\rho_{11}^{(2)}\right|^2 - \left|\rho_{S/AS}^{(3)}\right|^2\right| / \left|\left|\rho_{11}^{(2)}\right|^2 + \left|\rho_{S/AS}^{(3)}\right|^2\right|. \quad (7)$$

The values of C indicate the quality of interference. The two-mode intensity-noise correlation function $G_{FL}^{(2)}(\tau)$ between intensity fluctuations of two optical beams $i, j, (i \neq j)$ as a function of time position τ is given by,

$$G_{ij}^{(2)}(\tau) = \frac{\left\langle \delta\hat{I}_i(t_i)\delta\hat{I}_j(t_j)\right\rangle}{\sqrt{\left\langle [\delta\hat{I}_i(t_i)]^2\right\rangle\left\langle [\delta\hat{I}_j(t_j)]^2\right\rangle}}$$
$$= [|R_E R_C|^2 e^{-2\Gamma_{ij}^+|\tau|} + e^{-2\Gamma_{ij}^-|\tau|}$$
$$- 2\cos(\Omega_e|\tau|)e^{(\Gamma_{ij}^+ + \Gamma_{ij}^-)|\tau|}] \qquad (8)$$

where R_E and R_C are constants, and the line shape of the correlation function is mainly affected by the decay rate Γ, while $\delta\hat{I}_i(t_i)$ and $\delta\hat{I}_j(t_j)$ are the intensity fluctuations of E_{AS} and E_S signals, respectively. In the case of two FL signals, Eq. (9) can be rewritten as [26]

$$G_{FL}^{(2)}(\tau) = \left\langle \delta\hat{I}_i(t_i)\delta\hat{I}_j(t_j)\right\rangle \propto 1 + sinc^2(\Gamma_{FL}\tau/2) \quad (9)$$
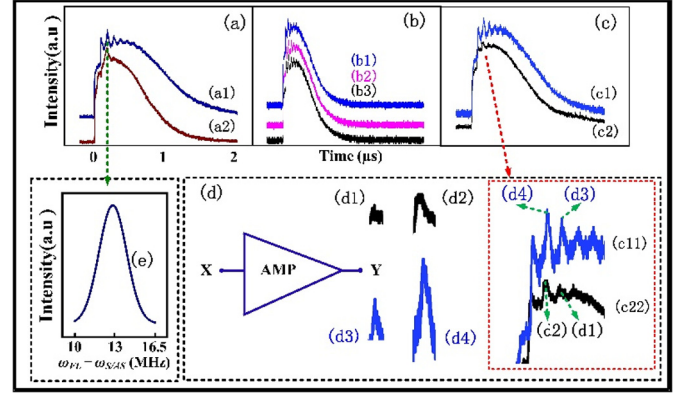

Fig. 2. Fig. 2 shows the temporal comparison of oscillations obtained from mixed-phase (T + H) Eu^{3+}: YPO_4. (a1) and (a2) outputs detected at PMT1 and PMT2 at 300 K, respectively. (b) oscillations are measured at different temperatures. (c1) and (c2) oscillations obtained at resonant and off-resonant wavelength, respectively. (d) shows a diagram of the temporal amplifier and (c11, c22) is the zoom part of temporal signal from (c1, c2), respectively. Fig. 2(d1-d2, d3-d4) are truncated from corresponding Fig. 2(c11, c22), respectively. (e) represents Fourier transform corresponding to Fig. 2(a1).

4. Results and discussion

Fig. 2 shows the temporal comparison of oscillations obtained from mixed-phase (T + H) Eu^{3+}: YPO_4. Fig. 2(a1) and 2(a2) show the temporal intensity of the hybrid signals H_1 and H_2, respectively. The output hybrid signals H_1 and H_2 are generated at a low input beam power of 1 mW. Oscillations resulted from the interference of FL and E_S/E_{AS} in a hybrid signal regime is called interference oscillation, which is realized through nonlinear interaction [22]. The intensity of FL can be written as $I_{(FL)} \propto \left|\rho_{11(FL)}^{(2)}\right|^2$. The intensity functions mentioned in Eqs. (3) and (4) show Cosine oscillation in the time-domain and are exponentially damped. The time-domain signal detected at PMT1 (Fig. 2(a1)), frequency $(\omega_{FL} - \omega_{S/AS})$ (Fig. 2 (e)) of interference oscillation is high as compared with that detected at PMT2 (Fig. 2(a2)). This can be explained by the interference between FL and E_S (FL and E_{AS}) in hybrid signal H_1 (H_2), from Cosine oscillation in the time domain $\cos[(\omega_{FL} - \omega_{S/AS})t]\exp[-(\Gamma_{FL} + \Gamma_{S/AS})t]$ modeled by Eq. (6). The decay rate of interference hybrid signal is given by $\Gamma_{FL} + \Gamma_{S/AS}$. At PMT1, the hybrid signal H_1 contains more FL. Hence, the interference between FL and E_S is almost equal due to the equal emission of FL and E_S in a hybrid signal H_1, which results in strong interference oscillation (Fig. 2(a1)). The temporal signal obtained at PMT2 results in low interference oscillation as shown in Fig. 2(a2), which is due to less interference between FL and E_{AS}. On the other hand, when the dressing effect $(\Delta_1 - |G_1|^2/\Gamma_{00})$ in Eq. (5) is strong, we cannot observe self Rabi-oscillation due to the longer period of Stokes in Fig. 2(a2). As compared to the NV center [24], Eu^{3+}: YPO_4 crystal has a strong dressing effect because of the high dipole moment. In Fig. 2(b), the hybrid signal H_1 at PMT1 is recorded by decreasing temperature from 160 K to 77 K, the graphs suggest temperature dependence of temporal oscillations. When the temperature is at 160 K, the phonon effect is dominant, and the dressing effect is less, which results in a low frequency of oscillation in Fig. 2(b1). As temperature decreases, interference of FL and E_S appears in hybrid signal H1 in Fig. 2(b2). By decreasing temperature to 77 K, the phonon effect decreases, and dressing increases, where interference between FL and E_S increases slightly in hybrid signal H_1 in Fig. 2(b3). Hence oscillation observed at 77 K (Fig. 2(b3)) is slightly stronger than oscillation observed at 160 K (Fig. 2(b1)). In Fig. 2(c), we study the dependence of self-Rabi oscillations in hybrid signal H_2 (PMT2) via resonant and off-resonant excitations. For resonant excitation
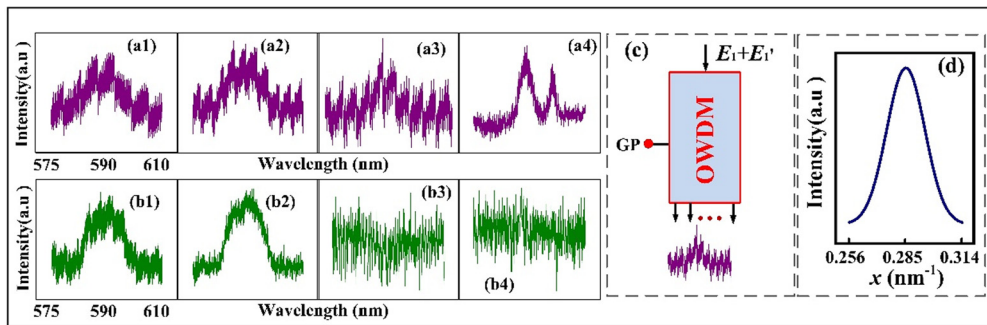
Fig. 3. (a) and (b) show the spectral signal from the mixed phase (much-T + less-H) Eu^{3+}: YPO_4 by changing gate position (GP) from t_1 to t_4 (200 ns, 600 ns, 1 μs, 5 μs), (c) shows wavelength division multiplexing function, where output spectral interference signal corresponds to Fig. 3(a3). (d) represents Fourier transform corresponding to Fig. 3(a3).

shown in Fig. 2(c1), the self Rabi-oscillations were observed from Eq. (4) due to the strong dressing effect. By changing frequency detuning from resonant to off-resonant, the dressing in a hybrid signal H_2 becomes minimum, and less self Rabi-oscillation is observed in Fig. 2(c2). This can be explained by the dressing effect $|G_1|^2/(\Gamma_{10} + i\Delta_1)$ since the dressing effect at resonant excitation is more than that at the off-resonant excitation. Hence, we can conclude that self Rabi-oscillation is observed robust and prominent with resonant excitation (Fig. 2(c1)) when compared with off-resonant excitation (Fig. 2(c2)).

Using Fig. 2(c1) and 2(c2), we realized the temporal amplifier for time-domain results at resonant and off-resonant frequency. The model of the temporal amplifier is shown in Fig. 2(d), where the signal at off-resonant (Fig. 2(c2)) is an input temporal signal (X), E_1 is a control signal (analogous to the base current BJT), Y is the output of the temporal amplifier, G is gain and N is the internal noise of the temporal amplifier. Therefore, we mathematically model the output of the temporal amplifier as Y = G*X + N. At first, when the frequency of E_1 is set to off-resonant the amplitude of temporal signal peak is low as shown in Fig. 2 (d1 and d2). When frequency of E_1 changes to resonant the intensity of temporal signal peaks increases and becomes more prominent as shown in Fig. 2(d3 and d4). At resonant frequency the peaks are amplified to maximum due to high gain (G = Y/X > 1) caused by strong dressing effect.

Next we discuss the interference oscillations for spectral results obtained at two different detectors PMT1 and PMT2 with respect to change in gate position of a boxcar gate.

Fig. 3 shows the spectral intensity from the mixed phase (much-T + less-H) Eu^{3+}: YPO_4. The hybrid signal H_1 and H_2 were recorded at PMT1 and PMT2, at different gate positions (200 ns, 600 ns, 1 μs, 5 μs) by scanning E_1 from 575 nm to 610 nm. In Fig. 3, the excitation spectrum is measured when the power of the input beam is kept at medium power (4 mW) while the temperature is set to be 77 K. By maintaining power at 4 mW, only oscillation from interference is observed in Fig. 3. The interference oscillation increases due to increase in interference between FL and $E_{S/AS}$ in a hybrid signals H_1 and H_2. The hybrid interference frequency can be associated with the decay rates (Γ_{FL} and $\Gamma_{S/AS}$) of $\cos[2\pi c/\lambda(1/\Gamma_{FL} - 1/\Gamma_{S/AS})]$ from Cosine oscillation in spectral-domain modeled by Eq. (6). The spectral peak with broad linewidth can be attributed to the FL signal because of a low lifetime. Contrary to FL, the SP-FWM signals are generated from the coherent process; hence their linewidth is determined by the atomic coherence time and is much narrower. The sharp peak in Fig. 3(a4) (Fig. 3(b4)) observed at gate position t_4 can be attributed to Stokes (anti-stokes) signals. As explained above, since the change in gate position corresponds to different energy levels with different lifetime, the interference between FL and Stokes in a hybrid signal can be controlled by changing gate position. When

the gate position is fixed at t_1 (200 ns), the spectral signal of broad linewidth (17 nm) with interference oscillation is observed in Fig. 3(a1). At t_1, E_S emission is very weak as compared to FL in a hybrid signal H_1; hence, the frequency of oscillation resulted from the interference between FL and E_S is low in Fig. 3(a1). When the gate position is changed to t_2 (600 ns) the emission of E_S is slightly increased in H_1, resulting in a bit higher frequency of interference oscillations that can be observed in spectral domain as shown in Fig. 3(a2). When the gate position is changed to t_3 (1 μs), the contribution of FL and E_S emission is almost equal in hybrid signal H_1, which corresponds to a maximum interference between FL and E_S, as a result, the oscillation frequency in spectral signal will be high in Fig. 3(a3), which is similar to the temporal signal shown in Fig. 2(a1). Fig. 3(d) shows the Fourier transform corresponding to Fig. 3(a3). Further by changing gate position to t_4 (5 μs), E_S emission dominates over FL in H_1 due to the short lifetime of FL. Here, the emission of FL in hybrid signal is negligible, so no interference oscillation is observed, where the spectral signal with two sharp resonant peaks is observed in Fig. 3(a4). Fig. 3(b) follows the similar behavior of spectral hybrid signal H_2 according to the change in gate position, as explained in Fig. 3(a). Here, E_{AS} emission is more than FL in hybrid signal H_2 which is subjected to the far position of PMT2. When the gate position is fixed at t_1, the hybrid signal H_2 has a slight FL emission, resulting in a low oscillation frequency in Fig. 3(b1), similar to that in Fig. 2(a2). While when the gate position is changed to t_2, E_{AS} dominates over FL emission corresponding to weak interference and low frequency of oscillation in Fig. 3(b2). Furthermore, by increasing the gate position to t_3 and t_4, the hybrid signal is dominating by E_{AS} emission, and the FL emission is almost negligible, resulting in no interference in the hybrid signal, hence, no interference oscillation could be observed in Figs. 3(b3) and 3(b4).

Here, we have realized the wavelength division multiplexing of classical and coherent channels. From t_1 to t_3, the classical FL can be multiplexed with various divided peak for classical channel, which can help in routing the same information from seven (Fig. 3(a1)) to nine channels (Fig. 3(a2)), and to ten channels (Fig. 3(a3)). This realization of WDM is achieved by changing the boxcar gate position. Similarly, when gate position is placed at t_4, the coherent channel output can be multiplexed to two divided peaks for routing same information to different channels. Fig. 3(a1-a4) show two adjacent peaks relative distance between many peaks. Such a phenomenon is analogous to routing the same peak information. Here we use channel equalization ratio ($P = 1 - \sqrt{\sum_1^{N-1}(s_i - a)^2/a}$) to measure the WDM, where a is the area of one peak and s_i is the area of each peak or gap between peaks. When $s_i \approx a$, P will be maximum (100%) and we will get more balanced and stable spatial channels. From Fig. 3(a1-a3), channel equalization ratio P can approach 65% - 85%.
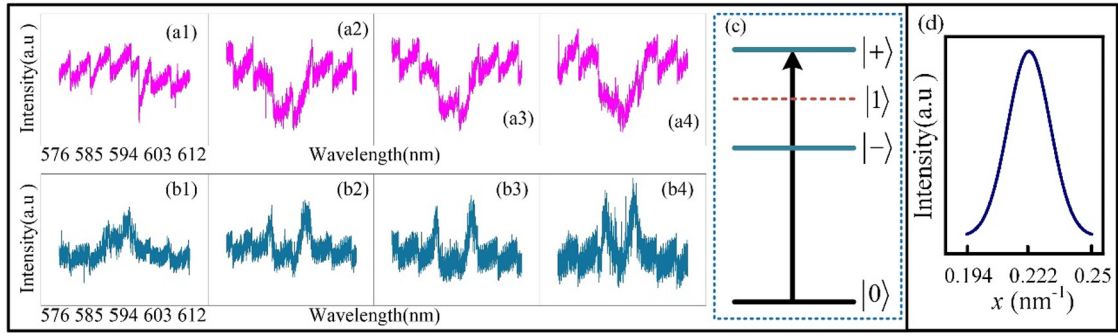
Fig. 4. (a) and (b) show a spectral-domain signal for mixed-phase (much-T + less-H) Eu^{3+}: YPO_4 by decreasing the temperature of cryostat from high to low (220 K, 150 K, 100 K, 77 K), detected at PMT1 and PMT2, respectively. (c) shows the dressed energy levels and (d) represents Fourier transform corresponding to Fig. 4(a1).

Next, we discuss the interference oscillations for spectral results obtained at two different detectors PMT1 and PMT2 with respect to temperature.

The spectral intensity signal in Fig. 4 is plotted by changing temperature from high to low (220 K, 150 K, 100 K, 77 K) when the gate position is fixed at 200 ns while E_1 power is fixed high (7 mW). By changing the temperature from 220 K to 77 K, there is no change in the frequency of interference, and oscillations are observed in Figs. 4(a) and 4(b). When the temperature decreases, the proportion of both FL (Γ_{FL}) and SP-FWM ($\Gamma_{S/AS}$) equally changes in term $\cos[2\pi c/\lambda(1/\Gamma_{FL} - 1/\Gamma_{S/AS})]$ as in Eq. (6), and the hybrid interference between FL and SP-FWM remains consistent. The interference at 77 K (Figs. 4(a4) and 4(b4)) is almost equal to the interference at 220 K (Figs. 4(a1) and 4(b1)). Hence in Fig. 4, the frequency oscillation from the interference between FL and $E_{S/AS}$ in a hybrid signal (H_1/H_2) is independent of temperature. In addition, no change in the interference oscillations (Fig. 4(d)) is observed by decreasing temperature in Figs. 4(a) and 4(b), while the dressing effect $|G_1|^2/(\Gamma_{10} + i\Delta_1)$ in Eq. (5) increases, which increases the amplitude of the spectral signal. The spectral signal in Fig. 4(a) is detected at PMT1, where FL emission is more than E_S in a hybrid signal H_1. When the temperature is fixed at 220 K, the broad spectral signal is observed in Fig. 4(a1). When the temperature decreases from 220 K to 77 K, the dressing effect increases, which increases the amplitude of the spectral signal in Fig. 4(a1-a4) and Fig. 4(b1-b4). Furthermore, a pure dressed suppression profile dip appears in Figs. 4(a2), 4(a3), and 4(a4), owing to the dressed suppression condition $\Delta_1 = 0$ of dressing effect ($|G_1|^2/(\Gamma_{10} + i\Delta_1)$) mentioned in Eq. (5). Further, in Fig. 4(b) we observe spectral Autler-Townes (SAT)-splitting in Figs. 4(b2)-4(b4) detected at PMT2 unlike to Fig. 4(a). The less dressing effect can be explained due to the low FL emission as compared with E_{AS} in a hybrid signal H_2 at PMT2. The SAT-splitting correspond to the dressed state $|\pm\rangle$ created by E_1. The self-dressing field E_1 splits the state $|1\rangle$ into two dressed states $|+\rangle$ and $|-\rangle$ as shown in Fig. 4(c). By using Hamiltonian ($H|\pm\rangle = \lambda_\pm |\pm\rangle$), SAT-splitting distance can be written as $\Delta_\pm = \lambda_+ - \lambda_- = (\Delta_1^2 + 4|G_1|^2)^{1/2}$, where the splitting distance $\Delta_\pm$ is proportional to the dressing effect $|G_1|^2$. When the temperature is high, the phonon effect (Γ_{phonon}) is high, and the phonon is related to $\Gamma_{ij} = \Gamma_{pop} + \Gamma_{ion-spin} + \Gamma_{ion-ion} + \Gamma_{phonon} - \Gamma_{dressing}$. Hence, Γ_{10} in dressing term $|G_1|^2/(\Gamma_{10} + i\Delta_1)$ of Eq. (5) can be controlled by temperature. The high temperature leads to increases in phonon effect, suggesting high Γ_{10}, which consequently reduces the dressing effect, in temporal signal as mentioned above in Fig. 2(b). Hence, by fixing temperature at 220 K, no SAT-splitting is observed in Fig. 4(b1) due to low dressing effect. By decreasing temperature from 220 K, the phonon effect reduces, which increases the dressing term $|G_1|^2/(\Gamma_{10} + i\Delta_1)$ in Eq. (5). Hence, the profile of the hybrid signal evolves from the SAT-splitting peak to a mixture of SAT-splitting and small suppression dip in Figs. 4(b2) and
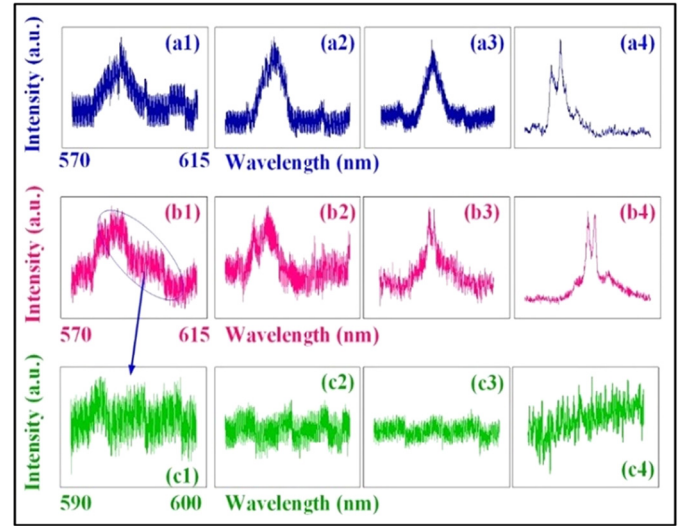

Fig. 5. (a) and (b) show the spectral domain signal recorded at PMT2 from pure H-phase of Eu^{3+}: YPO_4 and Pr^{3+}: YPO_4, respectively, by changing gate position from t_1 to t_4 (1 μs, 7 μs, 20 μs, 50 μs). (c) shows a specific part of (b) where oscillation can be observed.

4(b3). When the temperature reaches to 77 K, the SAT-splitting becomes obvious in Fig. 4(a4). This suggests that at low temperature, FL ($\rho_{FL}^{(2)}$) evolves from SAT-splitting caused by the dressing effect of E_1 by the term $|G_1|^2/(\Gamma_{10} + i\Delta_1)$ in Eq. (5). At a low temperature of 77 K, SAT-splitting increases due to an increase in SAT-splitting distance $\Delta_\pm$ caused by the dressing term $|G_1|^2$ as shown in Fig. 4(b4). Unlike Fig. 4, no suppression dip or SAT-splitting is observed in Fig. 3, which can be explained by low power excitation of E_1 in Fig. 3, which resulted in weak dressing effect.

Next, we investigate the interference oscillation from two different materials (Pr^{3+}: YPO_4 and Eu^{3+}: YPO_4), obtained from PMT2 by changing the gate position of boxcar gate.

In Fig. 5, by changing gate position from t_1 to t_4 (1 μs, 7 μs, 20 μs, 50 μs), FL emission in a hybrid signal H_2 gradually changes to E_{AS}, predicted by change in the linewidth of spectral signal from broad (Fig. 5(a1)) to sharp (Fig. 5(a4)). The frequency oscillation in spectral intensity signal resulted from the interference between FL and E_{AS} in a hybrid signal regime is similar, as explained in Fig. 3. When the gate position is fixed at t_1 (1 μs), the spectral signal of Eu^{3+}: YPO_4 with broad linewidth and oscillation is observed in Fig. 5(a1). As we explained in Fig. 3 that as the FL emission at PMT2 is very weak, the interference between FL and E_{AS} in a hybrid signal H_2 results in low oscillation (Fig. 5(a1)). By changing the gate position to t_4 (50 μs), the FL emission in H_2 is negligible, and therefore, the spectral signal with sharp resonant peaks (no oscillations) is observed in Fig. 5(a4). Furthermore, Fig. 5(b)
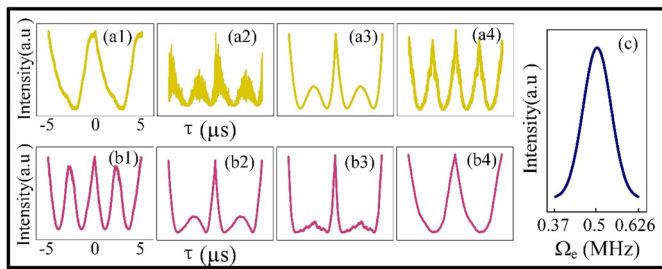
Fig. 6. Fig. 6 shows a two-mode intensity noise correlation between hybrid signals H_1 and H_2 from the mixed phase (much-T + less-H) Eu^{3+}: YPO_4. (a) shows the two-mode intensity noise correlation at low power (1 mW) by changing gate position t_i (200 ns, 600 ns, 1 μs, 5 μs). (b) shows the intensity noise correlation by decreasing power of E_1 from high to low (7 mW, 5 mW, 3 mW, 1 mW) when the gate position is fixed at 200 ns. (c) shows the Fourier transform of Fig. 6(a2).

follows a similar behavior of spectral hybrid signal with respect to the change in gate position as explained for Fig. 5(a) of Eu^{3+}: YPO_4. In Fig. 5(b), the interference between FL and E_{AS} in a hybrid signal H_2 is the same for different gate positions (t_1-t_4) as for Fig. 5(a).

When compare the H-phase of Eu^{3+}: YPO_4 (Fig. 5(a)) with that of Pr^{3+}: YPO_4 (Fig. 5(b)), we can conclude that the frequency of the self Rabi-oscillation is higher for Pr^{3+}: YPO_4 (Fig. 5(b1)) than for Eu^{3+}: YPO_4 (Fig. 5(a1)). This can be explained from the effect of different ion (Eu^{3+} and Pr^{3+}) in YPO_4. Both ions have different dipole moments, which can be calculated by $\mu = \sqrt{\varepsilon_0 h \Gamma \lambda^3 / 16 \pi^3 n_0^3}$, where ε_0 is the permittivity (8.85×10^{-12} F/m), h is Planck's constant (6.67×10^{-34} Js), while λ, Γ and n_0 are the laser wavelength, spectral linewidth and refractive index of Eu^{3+}: YPO_4 and Pr^{3+}: YPO_4, respectively. Here, the symmetry of H-phase in both Pr^{3+}: YPO_4 and Eu^{3+}: YPO_4 is the same, whereas the dipole moment of Pr^{3+}: YPO_4 is higher than that of Eu^{3+}: YPO_4 [27]. Hence, due to strong dipole moment, strong dressing effect [27][28] is observed in Pr^{3+}: YPO_4, which results in high frequency of self Rabi-oscillation in spectral signal as shown in Fig. 5(b1). The observed self Rabi-oscillation in Fig. 5(b1) is due to the strong dressing effect of Pr^{3+}: YPO_4. Unlike Fig. 5(a), prominent oscillations are observed in Fig. 3(b), which can be explained by different phase symmetry, the spectral signal in Fig. 3 is obtained from mixed-phase (much-T + less-H), where the dressing effect is higher than pure H-phase (Fig. 5(a)).

To further explore the oscillation, we did experiment for two channels now and investigate two-mode correlation with respect to change in gate position and power of laser.

Here in Figs. 6(a) and 6(b), we investigated the two-mode intensity-noise correlation, by changing gate position from t_1 to t_4 and power from high to low, respectively. The correlation is obtained at PMT1 and PMT2 by using Eq. (8). According to Eqs. (8) and (9), the profile of correlation function $G_{ij}^{(2)}(\tau)$ evolves from Sinc to Cosine function, which simulates the cross Rabi-oscillation. When change the gate position from t_1 to t_4, FL emission in hybrid signals gradually changes to E_S and E_{AS} emissions, which changes the linewidth of the correlation signal from broad to sharp. At gate position t_1 (200 ns), FL emission is higher than E_S and E_{AS} at PMT1 and PMT2, respectively. Due to high FL emission coherence time becomes low, results in sharp linewidth of correlation signal (Fig. 6(a1)). The sharp correlation signal in Fig. 6(a1) is determined by the Sinc function $\sin c^2(\Gamma_{FL}\tau/2)$ in Eq. (9). By changing gate position to t_4 (5 μs), hybrid signals H_1 and H_2 behave as pure E_S and E_{AS} signals, respectively, with large coherence time, results in broad linewidth of correlation signal (Fig. 6(a4)), which can be determined by Cosine function $\cos(\Omega_e |\tau|)$ in Eq. (8). Hence, the evolution profile of correlation function changes from Sinc to Cosine function in Fig. 6(a1-a4). Fig. 6(c) represents the Fourier transform

of Fig. 6(a2). Furthermore, the cross Rabi- oscillation is observed in Fig. 6(a4) due to high E_S and E_{AS} emission on both PMT1 and PMT2, respectively. Fig. 6(b1-b4) show the same phenomenon of change in evolution profile of correlation function from cosine to Sinc function when the power of input beam E_1 decreases (7 mW, 5 mW, 3 mW, 1 mW). When power of input beam E_1 is high (7 mW), due to strong dressing effect FL emission at PMT1 and PMT2 suppressed to minimum, where hybrid signals H_1 and H_2 are dominating by E_S and E_{AS} emission, respectively [25]. High emission of E_S and E_{AS} results in large coherence time, broadening the linewidth of the correlation function, and thus, cross Rabi-oscillation is observed in Fig. 6(b1). By decreasing power to 1 mW, due to low dressing effect FL emission increases in H_1 and H_2, which make the linewidth of correlation signal to become sharp, with no cross Rabi-oscillation is observed in Fig. 6(b4).

5. Conclusion

In conclusion, we studied the oscillation generated from Eu^{3+}/ Pr^{3+}: YPO_4 in both time and spectral domain, caused by the interference of FL and SP-FWM in hybrid signal regime. The oscillation comparison between Eu^{3+}: YPO_4 and Pr^{3+}: YPO_4 in spectral domain was controlled by the phase transition and the boxcar gate position. We discussed the interference and self Rabi-oscillations coexisting in temporal and spectral intensity, and also elaborated the cross-Rabi oscillation in correlated light beams in a hybrid signal and the evolution of fluorescence (Sinc function) to SP-FWM (Cosine function) when the power of input beam changes from high to low. The interference between FL and Stokes in a hybrid signal and transition from Cosine to Sinc function could help us to realize the temporal amplifier and the wavelength division multiplexing.

CRediT authorship contribution statement

[a] These authors contributed equally to this work.

Declaration of competing interest

The authors declare that they have no known competing financial interests or personal relationships that could have appeared to influence the work reported in this paper.

Acknowledgements

References

[1] A.K. Parchur, A.I. Prasad, S.B. Rai, R. Tewari, R.K. Sahu, G.S. Okram, R.A. Singh, R.S. Ningthoujam, Observation of intermediate bands in Eu3+ doped YPO4 host: Li+ ion effect and blue to pink light emitter, AIP Adv. 2 (2012) 032119.

[2] X. Yang, X. Dong, J. Wang, G. Liu, Glycine-assisted hydrothermal synthesis of YPO4: Eu3+ nanobundles, Mater. Lett. 63 (2009) 629–631.

[3] C. Feldmann, T. Jüstel, C.R. Ronda, P.J. Schmidt, Inorganic luminescent materials: 100 years of research and application, Adv. Funct. Mater. 13 (2003) 511–516.

[4] J.C.G. Bünzli, C. Piguet, Taking advantage of luminescent lanthanide ions, Chem. Soc. Rev. 34 (2005) 1048–1077.

[5] H.H. Wang, A.J. Li, D.D. Du, F.Y. Fan, L. Wang, Z.H. Kang, Y. Jiang, J.H. Wu, J.Y. Gao, All-optical routing by light storage in a Pr3+: Y2SiO5 crystal, Appl. Phys. Lett. 93 (2008) 221112.

[6] A.V. Turukhin, V.S. Sudarshanam, M.S. Shahriar, J.A. Musser, B.S. Ham, P.R. Hemmer, Observation of ultraslow and stored light pulses in a solid, Phys. Rev. Lett. 88 (2001) 023602.

[7] C.G. Ma, A.V. Popov, A.S. Vanetsev, O.M. Gaitko, E.O. Orlovskaya, S. Lange, Y.V. Orlovskii, Vacuum ultraviolet spectroscopic analysis of Ce3+-doped hexagonal YPO4·0.8 H2O based on exchange charge model, J. Lumin. 152 (2014) 70–74.

[8] A.S. Vanetsev, E.V. Samsonova, O.M. Gaitko, K. Keevend, A.V. Popov, U. Mäe-org, H. Mändar, I. Sildos, Y.V. Orlovskii, Phase composition and morphology of nanoparticles of yttrium orthophosphates synthesized by microwave-hydrothermal treatment: the influence of synthetic conditions, J. Alloys Compd. 639 (2015) 415–421.

[9] Y. Hikichi, T. Sasaki, K. Murayama, T. Nomura, M. Miyamoto, Mechanochemical changes of Weinschenkite-type RPO4 · 2H2O (R = Dy, Y, Er, or Yb) by grinding and thermal reactions of the ground specimens, J. Am. Ceram. Soc. 72 (1989) 1073–1076.

[10] Y.X. Ni, J.M. Hughes, A.N. Mariano, Crystal chemistry of the monazite and xenotime structures, Am. Mineral. 80 (1995) 21–26.

[11] L. Mandel, E. Wolf, Coherence properties of optical fields, Rev. Mod. Phys. 37 (1965) 231–287.

[12] J. Liu, H. Zheng, H. Chen, Y. Zhou, F.L. Li, Z. Xu, The first- and second-order temporal interference between thermal and laser light, Opt. Express 23 (2015) 11868–11878.

[13] A. Schwarzkopf, D.A. Anderson, N. Thaicharoen, G. Raithel, Spatial correlations between Rydberg atoms in an optical dipole trap, Phys. Rev. A 88 (2013) 061406.

[14] S. Zhang, F. Raza, I. Ahmed, W. Li, K. Jin, Y. Zhang, Photon interference of second- and third-order correlation generated by two fluorescence sources, J. Phys. Commun. 3 (2019) 095003.

[15] G. Scarcelli, V. Berardi, Y. Shih, Can two-photon correlation of chaotic light be considered as correlation of intensity fluctuations?, Phys. Rev. Lett. 96 (2006) 063602.

[16] A. Valencia, G. Scarcelli, M. Dangelo, Y. Shih, Two-photon imaging with thermal light, Phys. Rev. Lett. 94 (2005) 063601.

[17] R.S. Bennink, S.J. Bentley, R.W. Boyd, "Two-Photon" coincidence imaging with a classical source, Phys. Rev. Lett. 89 (2002) 113601.

[18] R. Wang, F. Raza, R. Pang, A. Khan, H. Ullah, Y. Zhang, Multi-order quantum beating effect of three-photon temporal interference with nondegenerate fluorescence sources, Results Phys. 15 (2019) 102732.

[19] P.A.M. Dirac, The Principles of Quantum Mechanics, 4th edition, Oxford University Press (Clarendon), Oxford, England, 1958.

[20] R.P. Feynman, A.R. Hibbs, Quantum Mechanics and Path Integrals, McGraw-Hill Companies, New York, 1965.

[21] T.B. Pittman, D.V. Strekalov, A. Migdall, M.H. Rubin, A.V. Sergienko, Y.H. Shih, Can two-photon interference be considered the interference of two photons?, Phys. Rev. Lett. 77 (1996) 1917.

[22] H. Tang, I. Ahmed, P. Puttapirat, T. Wu, Y. Lan, Y. Zhang, E. Li, Investigation of multi-bunching by generating multi-order fluorescence of NV center in diamond, Phys. Chem. Chem. Phys. 20 (2018) 5721–5725.

[23] L. Allen, J.H. Eberly, Optical Resonances and Two-Level Atoms, John Wiley and Sons, New York, 1975.

[24] F. Raza, A. Imran, X. Li, W. Li, Y. Li, J. Mao, Y. Zhang, Multi-mode correlation with self- and cross-Rabi oscillation in a diamond nitrogen-vacancy center, Laser Phys. Lett. 16 (2019) 055402.

[25] H. Lan, C. Li, C. Lei, H. Zheng, R. Wang, M. Xiao, Y. Zhang, Competition between spontaneous parametric four-wave mixing and fluorescence in Pr3+: YSO, Laser Phys. Lett. 12 (2015) 015404.

[26] S. Zhang, F. Raza, H. Fan, Y. Feng, A. Imran, K. Li, Y. Zhang, Multi-channel optical router of coexisting two- and three-mode bunching, Phys. Scr. 94 (2019) 085503.

[27] F. Raza, H. Fan, H. Ullah, F. Nadeem, H. Ali, J. Li, Y. Zhang, Optical transistor and router application of Autler-Townes-splitting in various solid atomic-like media, Opt. Lett. 45 (2020) 240–243.

[28] H. Fan, F. Raza, I. Ahmed, K. Li, H. Ullah, Y. Zhang, Three-type Fano interference controlled by the phase transition of Eu3+/Pr3+: YPO4, New J. Phys. 22 (2020) 093008.